

Electronic Structure

OPEN ACCESS**TECHNICAL NOTE**

Diabatic potential energy surfaces and semiclassical multi-state dynamics for fourteen coupled $^3A'$ states of O_3

RECEIVED

1 August 2022

REVISED

15 September 2022

ACCEPTED FOR PUBLICATION

23 September 2022

PUBLISHED

21 November 2022

Original content from this work may be used under the terms of the [Creative Commons Attribution 4.0 licence](#).

Any further distribution of this work must maintain attribution to the author(s) and the title of the work, journal citation and DOI.

**Zoltan Varga** , **Yinan Shu** , **Jiaxin Ning** and **Donald G Truhlar** *

Department of Chemistry, Chemical Theory Center and Minnesota Supercomputing Institute, University of Minnesota, Minneapolis, Minnesota 55455-0431, United States of America

* Author to whom any correspondence should be addressed.

E-mail: truhlar@umn.edu**Keywords:** multi-state, dynamics, potential energy surfaces and couplings, adiabatic, diabatic, coherent switching with decay of mixing, neural networkSupplementary material for this article is available [online](#)

Abstract

Dissociation and energy transfer in high-energy collisions of O_2 play important roles in simulating thermal energy content and heat flux in flows around hypersonic vehicles. Furthermore, atomic oxygen reactions on the vehicle surface are an important contributor to heat shield erosion. Molecular dynamics modeling is needed to better understand the relevant rate processes. Because it is necessary to model the gas flows in high-temperature shock waves, electronically excited states of O_2 and O can be populated, and molecular dynamics simulations should include collisions of electronically excited species and electronically nonadiabatic collisions. This requires potential energy surfaces and state couplings for many energetically accessible electronic states. Here we report a systematic strategy to calculate such surfaces and couplings. We have applied this method to the fourteen lowest-energy potential energy surfaces in the $^3A'$ manifold of O_3 , and we report a neural-network fit to diabatic potential energy matrix (DPEM). We illustrate the use of the resulting DPEM by carrying out semiclassical dynamics calculations of cross sections for excitation of O_2 in $^3A'$ collisions with O at two collision energies; these dynamics calculations are carried out by the curvature-driven coherent switching with decay of mixing method.

1. Introduction

The first step in modeling electronically nonadiabatic processes is to obtain potential energy surfaces and the matrix elements coupling them. Such surfaces and couplings, however, has been lacking for most atmospheric species. The second step is molecular dynamics simulations. To facilitate the efficient calculation of many trajectories for such simulations, it is most useful if the potential energy surfaces and couplings are available as analytic fits, and analytic fitting is practical only if a diabatic basis is used as part of the fitting process. In a diabatic basis, the surfaces and couplings are represented by a geometry-dependent diabatic potential energy matrix (DPEM) that has diabatic potential energy surfaces on the diagonal and diabatic coupling matrix elements on the off-diagonal; the elements of a DPEM are smooth, facilitating the analytic representation [1]. A DPEM provides all the electronic structure information needed for modeling electronically inelastic processes. The present article introduces new methods involving DPEMs for fitting potential energy surfaces and applies them generate potential energy surfaces needed for dynamical modeling of electronically nonadiabatic collisions of atmospheric species.

Dissociation and energy transfer in collisions of O_2 play important roles in determining thermal energy content and heat flux in flows around hypersonic vehicles [2]. Furthermore, atomic oxygen reactions on the vehicle surface are an important contributor to heat shield erosion [3]. Molecular dynamics modeling is needed to better understand the relevant rate processes [4]. Because it is necessary to model the gas flows in high-temperature shock waves, electronically excited states of O_2 and O can be populated, and molecular

Table 1. The energy levels (with spin–orbit coupling removed) of $O_2 + O$ collision partners up to the dissociation energy of ground state $O_2(^3\Sigma_g^-)$ and the number of potential energy surfaces in each symmetry manifold associated with each asymptote.

Asymptote			Potential energy surfaces					
O_2	O	ΔE	Singlet		Triplet		Quintet	
		eV	$^1A'$	$^1A''$	$^3A'$	$^3A''$	$^5A'$	$^5A''$
$^3\Sigma_g^-$	3P	0.00	2	1	2	1	2	1
$^1\Delta_g$	3P	0.98			3	3		
$^1\Sigma_g^+$	3P	1.64			1	2		
$^3\Sigma_g^-$	1D	1.97			2	3		
$^1\Delta_g$	1D	2.94	5	5				
$^1\Sigma_g^+$	1D	3.61	3	2				
$^1\Sigma_u^-$	3P	4.10			2	1		
$^3\Sigma_g^-$	1S	4.19				1		
$^3\Delta_u$	3P	4.30	3	3	3	3	3	3
$^3\Sigma_u^+$	3P	4.39	1	2	1	2	1	2
$^1\Delta_g$	1S	5.17	1	1				
	Sum		15	14	14	16	6	6

dynamics simulations should include collisions of electronically excited species and electronically nonadiabatic collisions. However, the required surfaces and couplings have been available in neither adiabatic nor diabatic representations. Furthermore, the methods for generating electronically nonadiabatic potential energy surfaces for a large number of coupled surfaces have needed further development.

The present article provides a systematic strategy to calculate such surfaces and couplings. In addition to presenting the new strategy, we illustrate it by providing a 14×14 DPEM for the fourteen lowest-energy potential energy surfaces in the $^3A'$ manifold of O_3 , and we use this DPEM to provide initial estimates of cross sections for electronically nonadiabatic $O + O_2$ collisions.

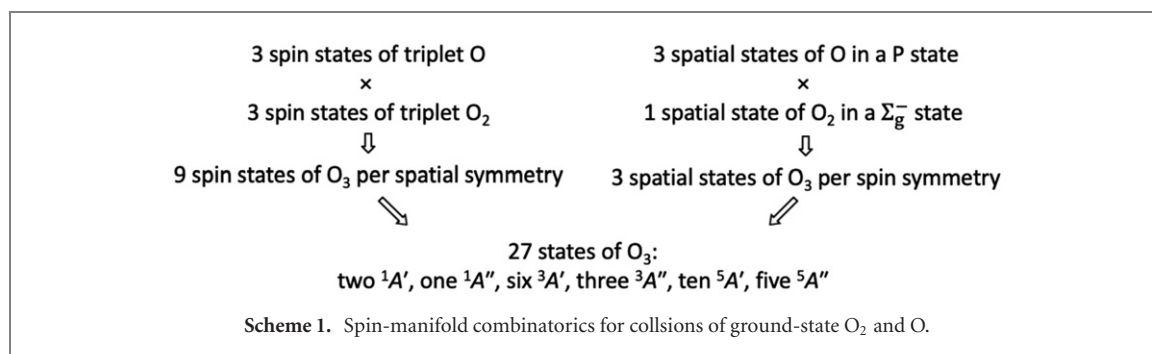
Although the motivation for the present work is the modeling of high-energy electronically inelastic collisions, we alert the reader to recent work [2, 5–17] on electronically adiabatic $O_2 + O$ collisions.

1.1. Potential surfaces involved in $O + O_2$ collisions

For oxygen atoms and molecules, the spin–orbit coupling is small, and we neglect it in the present study, so spin is taken to be a good quantum number. The collisions of ground-state or low-energy states of O_2 and O can occur in singlet, triplet, and quintet spin states, i.e., $S = 0, 1, 2$, where S is the quantum number of total electronic spin of the O_3 collision system. Since three atoms are always in a plane, C_s symmetry is a global symmetry. We neglect Coriolis coupling (which includes Renner–Teller interactions), so symmetry under reflection in the plane provides a good quantum number [18], and all electronic states have A' and A'' symmetry, which is conserved. Therefore, we have six uncoupled symmetry manifolds: $^{1,3,5}A'$ and $^{1,3,5}A''$.

States and energies of O_2 and O were obtained from references [19, 20], respectively. In the case of O atom, the energies were converted to spin–orbit-free values by removing spin–orbit coupling to first order in the usual way (this involves replacing the energy of the spin–orbit-split multiplet by the weighted average of the multiplet). Table 1 lists the possible combinations of the low-lying energy states of O_2 and low-lying energy states of O atom; these combinations provide the potential energy asymptotes of $O + O_2$ collisions. Table 1 considers all possible asymptotes up to the dissociation potential energy of ground-state O_2 , which is 5.2 eV. Table 1 also lists the number of states in each manifold that connect adiabatically to each possible asymptote.

In a gas of unoriented atoms and molecules (the usual case), the probability that a collision with a given asymptote (i.e., a given combination of O_2 and O electronic state symbols) initiates in a given spin manifold is proportional to the spin degeneracy (1, 3, or 5) of the spin manifold. Thus, for ground-state collisions, i.e., $O_2(^3\Sigma_g^-) + O(^3P)$ collisions, the probabilities of collisions as singlets, triplets, or quintets are 1/9, 1/3, and 5/9, respectively. In a given spin manifold, the probability of entering the interaction region of a binary collision on a given state of a degenerate level is the same for each state of a degenerate level [21]. The spin-manifold collision combinatorics for a collision of ground-state species is shown in scheme 1 to illustrate the general situation. Because, for collisions emanating from the lowest asymptote, the A' spatial manifolds each have two states (degenerate in the asymptotic region but not in the interaction region), it is equally likely for collisions to initiate on each of the two states; thus, for example, 1/9 of the collisions initiate in the $1^3A'$ state and 1/9



initiate in the $2^3A'$ state. More completely, again based on the first row of table 1, we have probabilities of 2/27, 1/27, 2/9, 1/9, 10/27, and 5/27 for the $^1A'$, $^1A''$, $^3A'$, $^3A''$, $^5A'$, $^5A''$ spatial-spin manifolds, respectively. Similar probabilities apply to the other asymptotes.

Calculating and fitting all the spatial-spin manifolds is a long-term goal; we start here with the most important manifold. Although the quintet spin manifold is the dominant one for the ground-state collisions, the table shows that the first three electronically excited asymptotes connect only to triplet states. Thus, the triplet spin manifolds are the most important ones for electronically nonadiabatic collisions that originate at the lowest asymptote, and two thirds of the ground-state triplet collisions occur in the $^3A'$ spatial-spin manifold. Therefore, we choose the $^3A'$ spatial-spin manifold for our first application of the new method presented here. Since table 1 shows fourteen $^3A'$ states in the energy range of interest, we consider the first fourteen states of the $^3A'$ manifold.

1.2. Choice of representation

The electronic structure calculations provide the potential energies of the O₃ states in the adiabatic representation. The fitting of potential energy surfaces and couplings in an adiabatic representation is not practically possible because of conical intersection seams where the potentials have cuspidal ridges and the nonadiabatic couplings (NACs) are singular vectors. In contrast, the diabatic potential energies are smooth and the couplings in the diabatic representation are smooth scalars. The diabatic potentials and diabatic couplings together form the DPEM. Because the elements of the DPEM are smooth functions of geometry, they are easier to fit than the adiabatic potentials [1]. If desired for dynamics calculations, the adiabatic energies, the gradients of the adiabatic energies, and NACs can be obtained from the DPEM; alternatively, the dynamics calculations may be carried out directly in the diabatic representation, with gradients of the diabatic potentials obtained analytically or numerically from the fit.

Obtaining the DPEM from the calculated adiabatic energies is called diabaticization, and many diabaticization techniques have been developed [1]. In the present work, a recently developed diabaticization technique is used, with new strategies as required to handle this very demanding case (we know only two previous diabaticizations that include such a high number of states [22, 23]). The diabaticization and the fitting is carried out by a deep neural network, and the method is called diabaticization by deep neural network (DDNN) [24]. The original DDNN method was recently extended to include restraints for invariance under permutation of identical atoms, leading to permutationally restrained DDNN [25], abbreviated PR-DDNN, and we use this feature for the present application to homonuclear O₃. A notable feature of the DDNN and PR-DDNN methods is that they are adiabatic equivalent, which means that the diabatic states span the same space as the adiabatic ones; this means that diagonalization of the 14×14 DPEM yields the fourteen lowest adiabatic potential energy curves.

1.3. Electronic structure calculations

The calculation of potential energy surfaces over broad regions of coordinate space including those with partially broken bonds requires a multireference treatment. We therefore use extended multi-state complete active space second-order perturbation theory (XMS-CASPT2) calculations [26, 27]. These calculations are based on a reference state obtained by a state-averaged complete-active-space self-consistent field calculation (SA-CASSCF [28–30]) in which the fourteen lowest $^3A'$ energies are minimized with equal weights. In the active space, 18 electrons were distributed in 12 orbitals corresponding to the valence shells (2s and 2p) of the oxygen atoms.

The gradients and the NAC vectors were also calculated at the SA-CASSCF level, but this is not needed for DDNN or PR-DDNN, and it was only used in a limited set of cases to verify the reasonableness of the assignments of the diabatic states along selected 1D paths through coordinate space.

Most calculations are carried out with C_s symmetry, as discussed in the introduction. For collinear and perpendicular-bisector geometries, symmetry under the C_{2v} point group was used to separate the fourteen $^3A'$ states into 3A_1 and 3B_1 submanifolds in which only states in the same submanifold can interact with each other. These C_{2v} calculations are used to help assign the diabatic states. Since the $^3A'$ states in C_s symmetry are ordered based on their energies, there are different numbers of 3A_1 and 3B_1 states in our 14 lowest $^3A'$ at different C_{2v} geometries; therefore, we must consider more than fourteen total states in the C_{2v} symmetry to be sure the fourteen lowest C_s states are included. For this reason, we calculated six 3A_1 and ten 3B_1 states for the collinear geometries and eight 3A_1 and eight 3B_1 states for the perpendicular-bisector geometries.

In the perturbation step, all electrons were correlated, an imaginary shift [31] of $0.1 E_h$ was applied, and the default IPEA shift ($0.25 E_h$) was used [32]. To obtain a basis set suitable for correlating all electrons, we combined weighted core-valence correlation [33] basis functions with minimal-augmentation [34] of diffuse functions to get the minimally augmented correlation-consistent polarized weighted core-valence triple zeta basis set (maug-cc-pwCVTZ) to describe the oxygen atoms.

All electronic structure calculations are performed with the 20.10 version (tag 30-ga1c588d-dirty) of the *OpenMolcas* program [35, 36].

1.4. Triatomic geometries used as input to the fit

There are two kinds of geometric input data to the PR-DDNN fit. The first kind is a set of geometries, $j = 1, 2, \dots, J$, each with the fourteen corresponding adiabatic energies. The second is the selection of a subset of these geometries, $k = 1, 2, \dots, K$, where the diabatic potentials are listed as restraints—further explanation of the choice of diabatic restraints is given below. In practice, $J \gg K$. This section describes the first kind of data.

Three sets of adiabatic energies were used. The first set consists of points on multidimensional grids. The multidimensional grids are described in appendix A. In trial calculations with only the multidimensional grid, we found that the fitted surfaces behaved unphysically at very short distances. (We had a similar experience when making a neural network fit of the N_4 system due to under sampling of certain geometry regions [37]). Therefore, we added some geometries with at least one very short bond length. These points are also described in appendix A. We also added some cuts defined in valence internal coordinates, also specified in appendix A.

1.5. Diatomic geometries used as input to the fit

XMS-CASPT2 calculations were also carried out for the potential energy curves of the ground and excited O_2 diatomic molecule. In these calculations, symmetry was turned off, the active space covers the valence electrons and valence orbitals, and the IPEA was set to be zero. The other options are the same as those for the O_3 calculations described above.

In one set of calculations, four singlet states were calculated to obtain the energy curves of the $^1\Delta_g$ and $^1\Sigma_g^+$, and $^1\Sigma_u^-$ states. In another set of calculations, four triplet states were calculated to obtain the energy curves of the $^3\Sigma_g^+$, $^3\Delta_u$, and $^3\Sigma_u^+$ states. Note that the Δ states are spatially doubly degenerate.

For the diatomic calculations, the bond length was varied from 0.6 to 4 Å with a 0.1 Å increment plus 5, 6, 7, 8, 9, and 9.99 Å. For each diatomic state, additional calculations were carried out in the vicinity of its equilibrium geometry with 0.01 Å increments.

1.6. Functional form of the DPEM

The three possible diatomic pairs are labeled 1, 2, and 3. The global (G) form of the DPEM at geometry j is expressed as

$$\mathbf{U}_j^G = \mathbf{U}^{2B}(r_{1j}, r_{2j}, r_{3j}) + \mathbf{U}^{MB}(r_{1j}, r_{2j}, r_{3j}) \quad (1)$$

where r_{ij} is the interatomic distance of diatom i at three-body geometry j , the two-body (2B) potential energy matrix is a sum of pairwise interactions (described below), and the many-body (MB) matrix (also described below) is the deviation from pairwise. The matrices in equation (1) have dimension $N \times N$, and in this work $N = 14$. The adiabatic potential energy matrix at geometry j are the diagonal elements of the diagonal matrix \mathbf{V}_j^G obtained by

$$\mathbf{V}_j^G = \mathbf{T}_j^\dagger \mathbf{U}_j^G \mathbf{T}_j \quad (2)$$

The zero of energy for the present surfaces corresponds to the energy of the $O_2(^3\Sigma_g^-) + O(^3P)$ asymptote with the bond length of O_2 set to the equilibrium value for the $^3\Sigma_g^-$ ground state.

1.7. Two-body potential energy matrix

We constructed the two-body potential energy matrix, \mathbf{U}^{2B} , to contain the pairwise contributions of the $\text{O}_2 + \text{O}$ state pairs shown in table 1 for the fourteen considered $^3A'$ states. We assume that, except for the ordering of the states, the diabatic potential energies are the same as the adiabatic potential energies in atom–diatom asymptotic regions (the DPEM is diagonal in asymptotic regions). Then the diatomic potentials are the diagonal elements $(\mathbf{U}^{2B})_{nn}$ of \mathbf{U}^{2B} , and the off-diagonal elements of \mathbf{U}^{2B} are zero. The diagonal element of \mathbf{U}^{2B} for state n is

$$(\mathbf{U}^{2B})_{nn} = V_0 + \sum_{i=1}^3 V_n^{\text{PA}}(r_{ij}) \quad (3)$$

where V_0 is a constant corresponding to the dissociation energy of ground state $\text{O}_2(^3\Sigma_g^-)$, and V_n^{PA} is the potential energy curve of state n .

In previous work, we already fit the pairwise potential of the ground state $\text{O}_2(^3\Sigma_g^-)$ to the sum of a short-range (SR) part and a dispersion term; see, for instance, references [5, 38, 39]. Generalizing this to state n gives

$$V_n^{\text{PA}} = V_n^{\text{SR}}(r_{ij}) + V^{\text{D3(BJ)}}(r_{ij}) \quad (4)$$

where the long-range term $V^{\text{D3(BJ)}}$ is a damped dispersion term based on Grimme's D3 dispersion parameters with the Becke–Johnson damping (BJ) function [40–42]. We used the same $V^{\text{D3(BJ)}}$ for all fourteen states.

The SR part in equation (4) is an even-tempered Gaussian expression. This function was originally used by Bytautas *et al* [43] to fit the whole potential energy curve of $\text{O}_2(^3\Sigma_g^-)$, and we used it in previous work to fit the V^{SR} part of the $\text{O}_2(^3\Sigma_g^-)$ potential energy curve. In the present work we also use this functional form to fit the excited-state O_2 potentials:

$$V_n^{\text{SR}} = \begin{cases} \left[\sum_{k=0}^7 a_{k,n} \exp(-\alpha_n \beta_n^k r_i^2) \right] + \left[\varepsilon_n \exp(-\delta_n (r_i - 1.7\text{\AA})^2) \right] & \text{if } n = 7, 8 \\ \sum_{k=0}^7 a_{k,n} \exp(-\alpha_n \beta_n^k r_i^2) & \text{if } n = 1 - 6 \text{ or } 9 - 14 \end{cases} \quad (5)$$

The target energies of V_n^{SR} for the SR fit were the differences between the adiabatic diatomic energies of V_n^{PA} and the energies of $V^{\text{D3(BJ)}}$. To get the target V_n^{PA} , first XMS-CASPT2 energies were calculated for the first four singlet and the first four triplet spin states of O_2 as described above. These two sets of calculations provide the curves of the $^1\Delta_g$, $^1\Sigma_g^+$, and $^1\Sigma_u^-$ states and the $^3\Sigma_g^-$, $^3\Delta_u$, and $^3\Sigma_u^+$ states, respectively. Since the $^3\Sigma_g^-$ was already described in previous works, that state was omitted in the following procedure; that curve corresponds to $n = 1, 2$ because table 1 shows that the lowest two potential surfaces of $^3A'$ O_3 dissociate to $\text{O}_2(^3\Sigma_g^-) + \text{O}(^3\text{P})$.

Based on the experimentally known energies of the states listed in reference [19], scaled external correlation [44] (SEC) was carried out to adjust the energies of the XMS-CASPT2 curves:

$$V_n^{\text{SEC}} = V_n^{\text{SA-CASSCF}} + F(V_n^{\text{XMS-CASPT2}} - V_n^{\text{SA-CASSCF}}) \quad (6)$$

where the parameter F was found to be 1.210 11, 1.294 035, 1.137 41, 1.2217, and 1.214 76 for the $^1\Delta_g$, $^1\Sigma_g^+$, $^1\Sigma_u^-$, $^3\Delta_u$, and $^3\Sigma_u^+$ states, respectively.

The XMS-CASPT2 calculations slightly overestimated the equilibrium bond lengths of the excited O_2 states with respect to the known values derived from experiment, and the SEC correction of equation (6) shifted these calculated values closer to the known values. To correct the remaining discrepancies, a few energies very close to the equilibrium geometry were shifted further to adjust the bottom of the energy curve to the known value. For states $^1\Delta_g$ and $^1\Sigma_g^+$, this shift is 0.002 Å; for state $^1\Sigma_u^-$, this shift is 0.007 Å; and for state $^3\Sigma_u^+$, this shift is 0.012 Å. For $^3\Delta_u$ only an estimate (1.48 Å) is available for the equilibrium bond length. This value seems to be too short and instead of using that value, we assumed a correction identical to that (0.012 Å) used for the $^3\Sigma_u^+$ state. The V_n^{SR} potential energy curves of excited O_2 were fitted using these SEC-corrected, equilibrium-corrected curves as target V_n^{PA} curves.

For states $n = 3, 4, 5, 6, 9, 10, 11, 12, 13, 14$, the excited O_2 molecule is combined with the ground-state $\text{O}(^3\text{P})$ atom. Since the energy of $\text{O}(^3\text{P})$ is zero (according to the triatomic zero of energy used here), it does not affect the energy of the O_2 molecule in the $\text{O}_2 + \text{O}$ system. Therefore, the energies of these states can be calculated from diatomic energy curves.

A special procedure is needed for the asymptotically degenerate $n = 7, 8$ potentials because they dissociate to the ground state of O_2 combined with the excited ^1D state of the atom (see table 1), and this special procedure is described in appendix B.

Table 2. Fitted parameters of V_n^{SR} for $n = 3-8$.

State	$n = 3, 4, 5$	$n = 6$	$n = 7, 8$
	$\text{O}_2(^1\Delta_g) + \text{O}(^3\text{P})$	$\text{O}_2(^1\Sigma_g^+) + \text{O}(^3\text{P})$	See text
$\alpha_n, \text{\AA}^{-2}$	0.926 743 129 655 067	0.859 772 042 751 452	2.191 857 281 503 71
$\beta_n, -$	1.493 100 945 033 26	1.523 763 358 517 61	-2663 791.408 822 74
$a_{0,n}, \text{kcal mol}^{-1}$	-288.154 824 977 704	-177.229 021 473 969	4890 643.134 805 23
$a_{1,n}, \text{kcal mol}^{-1}$	-1534.794 197 937 76	-1114.516 397 433 88	18 211 797.600 8347
$a_{2,n}, \text{kcal mol}^{-1}$	4738.544 133 528 97	2893.231 406 557 69	-69 478 406.883 1105
$a_{3,n}, \text{kcal mol}^{-1}$	-6160.202 918 065 25	-3085.763 750 683 64	88 925 293.456 462
$a_{4,n}, \text{kcal mol}^{-1}$	16 509.131 813 6742	13 366.332 675 3626	-48 996 476.314 9754
$a_{5,n}, \text{kcal mol}^{-1}$	-15 472.838 217 1874	-15 292.847 013 2772	7263 885.807 606 47
$a_{6,n}, \text{kcal mol}^{-1}$	47 185.693 365 4363	65 232.992 577 4647	1859 624.519 065 46
$a_{7,n}, \text{kcal mol}^{-1}$	-56 237.401 755 0829	-124 289.923 005 226	1.057 931 851 028 98
$\varepsilon_n, \text{kcal mol}^{-1}$			15.524 285 114 9696
$\delta_n, \text{\AA}^{-2}$			39.745 475 411 4259

Table 3. Fitted parameters of V_n^{SR} for $n = 9-14$.

State	$n = 9, 10$	$n = 11, 12, 13$	$n = 14$
	$\text{O}_2(^1\Sigma_u^-) + \text{O}(^3\text{P})$	$\text{O}_2(^3\Delta_u) + \text{O}(^3\text{P})$	$\text{O}_2(^3\Sigma_u^+) + \text{O}(^3\text{P})$
$\alpha_n, \text{\AA}^{-2}$	0.950 046 799 307	1.113 997 973 482 71	1.248 889 486 752 75
$\beta_n, -$	1.642 688 451 339	1.631 848 835 638 28	1.616 307 302 079 06
$a_{0,n}, \text{kcal mol}^{-1}$	-408.242 294 143 843	-511.287 998 639 776	-753.149 761 854 632
$a_{1,n}, \text{kcal mol}^{-1}$	506.602 117 753 963	1050.534 728 114 48	2601.163 394 524 51
$a_{2,n}, \text{kcal mol}^{-1}$	3224.661 234 888 42	4538.270 734 250 35	1889.443 031 421 37
$a_{3,n}, \text{kcal mol}^{-1}$	-2481.068 480 024 54	-6586.908 462 675 41	-692.325 517 266 325
$a_{4,n}, \text{kcal mol}^{-1}$	39 820.226 871 3929	36 344.118 338 394	46 293.602 002 5018
$a_{5,n}, \text{kcal mol}^{-1}$	-274 901.008 455 779	9867.7681 689 3001	-50 650.163 337 684
$a_{6,n}, \text{kcal mol}^{-1}$	4805 910.073 313 95	-2502 205.956 985 73	-16 795 533.652 2413
$a_{7,n}, \text{kcal mol}^{-1}$	-208 131 033.883 674	186 852 078.118 477	2063 993 155.900 11

In tables 2 and 3, the fitted parameters of V_n^{SR} are summarized for $n = 3-14$. For these parameters, the unit of the input bond length is \AA and the resulting energy is in kcal mol^{-1} . For $n = 1, 2$, the parameters of V_n^{SR} for ground state $\text{O}_2(^3\Sigma_g^-)$ potential can be found in Ref. 38. (In that case, the unit of the input bond length is \AA and the resulted energy is in millihartrees.)

PR-DDNN method.

The diabaticization and surface fitting procedure used to obtain the 14×14 DPEM of the $^3A'$ manifold of O_3 was started with a preliminary version of the PR-DDNN code [24, 25] and finished with a significantly upgraded version of the code that uses the built-in improvements of the *PyTorch* machine learning library [45], the most important of these improvements being the limited-memory Broyden-Fletcher-Goldfarb-Shanno (L-BFGS) algorithm [46]. The introduced algorithmic changes do not affect the description of the PR-DDNN method, but the efficiency of the processing is significantly increased; for instance, the evaluation time of an iteration is 12.5 times faster, and the L-BFGS algorithm is more robust. The effect of these changes will be discussed in a later section.

The neural network used in the PR-DDNN method is a fully connected feedforward L -layer network that has an input layer \mathbf{a}^1 , several hidden layers \mathbf{a}^2 to \mathbf{a}^{L-2} , a DPEM layer \mathbf{a}^{L-1} , and an adiabatic potential energy layer \mathbf{a}^L . The adiabatic layer is obtained by diagonalizing the DPEM. The general structure of the network up to the layer before the DPEM layer is given by

$$\mathbf{a}^{l+1} = g(\mathbf{z}^l) = g\left[(\mathbf{W}^l)^T \mathbf{a}^l + \mathbf{b}^l\right], \quad l = 1, 2, \dots, L-3 \quad (7)$$

where l is the index of a layer, T denotes a transpose, \mathbf{W}^l and \mathbf{b}^l are respectively the weight matrix and biases vector of layer l , and g is the activation function. In this work, the Gaussian error linear unit (GELU) activation function [47] is used:

$$g = \frac{1}{2} z_m^l \left(1 + \text{erf} \left(\frac{1}{\sqrt{2}} z_m^l \right) \right) \quad (8)$$

where z_m^l is element m of the M -dimensional vector \mathbf{z}^l , and erf denotes the error function. The activation function for the DPEM layer is the identity function.

If the input data, \mathbf{a}^l , has a wide range of values, neural network fits with the usual randomly initialized weights and biases sometimes encounter difficulties such as a slow or unstable learning process. These performance issues can be significantly decreased if the input variables are re-scaled to be numerically between 0 and 1. Therefore, we re-scaled the internuclear distances, r_i , where i equals 1, 2, or 3 and denotes a diatomic pair. At the beginning of this project, the Simons–Parr–Finlan (SPF) function [48] was used, and an element of \mathbf{a}^l was calculated by:

$$a_i^{1,\text{SPF}} = \frac{r_i - r_c}{r_i} \quad (9a)$$

where r_c is 1.511 78 bohr (corresponds to 0.8 Å). These SPF coordinates were used in the 1D, 2D, and some of the stage-by-stage global fits (explained below) to get the diabatic restraints for the final fit. But at the end of the fitting, we switched to exponentials of the internuclear distances:

$$a_i^{1,\text{Exp}} = \exp(-r_i/a_0) \quad (9b)$$

where a_0 is 1 bohr (~ 0.5292 Å). The final fit was carried out with these $a_i^{1,\text{Exp}}$ input coordinates.

Scaling could also be applied to the target data of the neural network, but we use relative energies in units of eV, which puts the target data in a numerically reasonable range, so no scaling was applied.

The currently used input coordinates ($a_i^{1,\text{SPF}}$ or $a_i^{1,\text{Exp}}$) are unitless. For the sake of convenience, one can also consider that the weights and biases are unitless. Since the elements in the DPEM have energy units, a convenient place to introduce the unit is last activation function right before the DPEM; as mentioned above, this activation function is an identity function.

1.8. Diabatic restraints

As already mentioned, the input to the PR-DDNN method includes the specification of a K -member subset (with index k) of the input geometry points at which the diabatic states are restrained to be close to a set of target diabatic energies. These restraints guide the fit to the adiabatic energies such that the adiabatic energies (which are not necessarily slowly changing functions of geometry) are obtainable from a set of diabatic states that are slowly varying functions of geometry. Because the restraint geometries k constitute a subset of the full set of geometries j , the elements of \mathbf{a}^l and \mathbf{z}^l , can have not only j indices as subscripts but also k indices. The \mathbf{a}_j^l vector consists of N perceptrons (here $N = 14$, i.e., the number of states) in layer L for each geometry j .

Since the DPEM is a symmetric matrix, the number N_{DPEM} of its unique elements is $\frac{1}{2}N(N+1)$, and these are stored as a string, where the first N elements are the diagonal elements of the DPEM and remaining $\frac{1}{2}N(N-1)$ elements are the upper triangular part of the DPEM. Therefore, the string representing the target DPEM of geometry k is stored as a vector Ξ_k^G . For a 14-state case, the DPEM layer has 105 elements. The vector \mathbf{a}_k^{L-1} consists of N_{DPEM} perceptrons in layer $L-1$ for each restraint geometry k .

The PR-DDNN method minimizes the following loss function:

$$\begin{aligned} c_{\text{PR-DDNN}} = & \frac{1}{2JN} \sum_{j=1}^J |\mathbf{a}_j^L - \mathbf{V}_j^G|^2 + \frac{\alpha_1}{2KN} \sum_{k=1}^K |\mathbf{a}_k^{L-1} - \Xi_k^G|^2 \\ & + \frac{\alpha_2}{2} \sum_{l=1}^{L-2} \sum_{\beta} \sum_{\beta'} |w_{\beta\beta'}^l|^2 + \frac{\alpha_3}{2J'JN} \sum_{j=1}^J \sum_{s=1}^{J'} |\mathbf{a}_{j_s}^L - \mathbf{V}_j^G|^2 \end{aligned} \quad (10)$$

where the third term is designed to prevent overfitting, and the fourth term promotes permutational invariance; α_1 , α_2 , and α_3 are adjustable parameters which we set equal to 1.0, 10^{-4} , and 1.0, respectively; $w_{\beta\beta'}^l$ is a matrix element of the weight matrix of hidden layer l ; s is the index of a permutation of identical nuclei; and J' is the number of possible permutations. For the O_3 system, there are three transpositions and two cyclic permutations of the O atoms, thus $J' = 5$.

As discussed below, the fitting involves a one-dimensional (1D) stage, a two-dimensional (2D) stage, and a global stage. We used equation (10) for the first two stages and all but the final step of the global stage. For the final fit, however, the two-body terms were separated from the many-body terms in the fitting procedure. According to this, $c_{\text{PR-DDNN}}$ is replaced by $c_{\text{PR-DDNN}}^{2\text{B}+\text{MB}}$:

$$\begin{aligned} c_{\text{PR-DDNN}}^{2\text{B}+\text{MB}} = & \frac{1}{2JN} \sum_{j=1}^J |\mathbf{a}_j^{L,2\text{B}+\text{MB}} - \mathbf{V}_j^G|^2 + \frac{\alpha_1}{2KN} \sum_{k=1}^K |(\mathbf{a}_k^{L-1,\text{MB}} + \Xi_k^{2\text{B}}) - \Xi_k^G|^2 \\ & + \frac{\alpha_2}{2} \sum_{l=1}^{L-2} \sum_{\beta} \sum_{\beta'} |w_{\beta\beta'}^{l,\text{MB}}|^2 + \frac{\alpha_3}{2J'JN} \sum_{j=1}^J \sum_{s=1}^{J'} |\mathbf{a}_{j_s}^{L,2\text{B}+\text{MB}} - \mathbf{V}_j^G|^2 \end{aligned} \quad (11)$$

where $\mathbf{a}_j^{L,2B+MB}$ is obtained by adding together the $\mathbf{a}_j^{L-1,MB}$ and Ξ_j^{2B} vectors and carrying out the operation that corresponds to diagonalization of DPEM, and Ξ_j^{2B} is the vector representation of \mathbf{U}^{2B} such that the first N elements of the vectors are the diagonal elements of \mathbf{U}^{2B} , (see equation (3)), and the other $\frac{1}{2}N(N-1)$ elements are zero. Because only the many-body part of the fit is carried out, the weights also get the MB superscript, $w_{\beta\beta'}^{l,MB}$. The global adiabatic energies \mathbf{V}_j^G and the global diabatic restraints Ξ_k^G remain the targets for this minimization problem.

The surface fit is carried out by optimizing the weights and biases of the network, and this is achieved by a backpropagation algorithm [49] by minimizing the cost function; the L-BFGS algorithm was used for this.

The numbers of weights and biases of the neural network are defined by the following equations:

$$N_w = \sum_{l=1}^{L-1} n_w^l n_w^{l-1} \quad (12)$$

$$N_b = \sum_{l=1}^{L-1} n_b^l \quad (13)$$

where n_w^l and n_b^l are the numbers of weights and biases, respectively, in layer l , and the total number of parameters, N_p , is the sum of the numbers of weights and biases.

$$N_p = N_w + N_b \quad (14)$$

The number of weights for the zeroth layer (n_w^{l-1} , where $l-1=0$) is equal to the number of input variables, for this system that is three (SPF or Exp variables obtained from the internuclear distances). We indicate the size and shape of a given five-layer neural network by $(n_w^0, n_w^{L-4}, n_w^{L-3}, n_w^{L-2}, N_{\text{DPEM}})$. The first number is size of the input vector, and the next three numbers are the numbers of neurons in the three hidden layers; these are user-defined numbers. The final number equals 105 to indicate the number of unique DPEM matrix elements.

1.9. Diabatic state ordering and the stages of the fit

Restraining the diabatic energies to be close to the adiabatic energies at K points is an essential part of the DDNN method, but it presents a complication in that the state order of the diabatic, and adiabatic energy lists can be different at some of these geometries. As an example of this complication, consider diabaticization along a 1D path with adiabatic potentials V_1 and V_2 and diabatic potentials U_{11} and U_{22} . Let us assume that there is a locally avoided state crossing between restraint points P_1 and P_2 along this path. Furthermore, assume that $V_1(P_1) \approx U_{11}(P_1)$, $V_2(P_1) \approx U_{22}(P_1)$, and $U_{12}(P_1) \approx U_{21}(P_1) \approx 0$. One might then have that $V_1(P_2) \approx U_{22}(P_2)$, $V_2(P_2) \approx U_{11}(P_2)$, and $U_{12}(P_2) \approx U_{21}(P_2) \approx 0$.

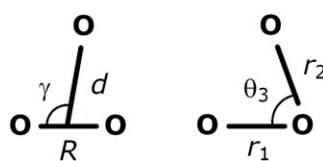
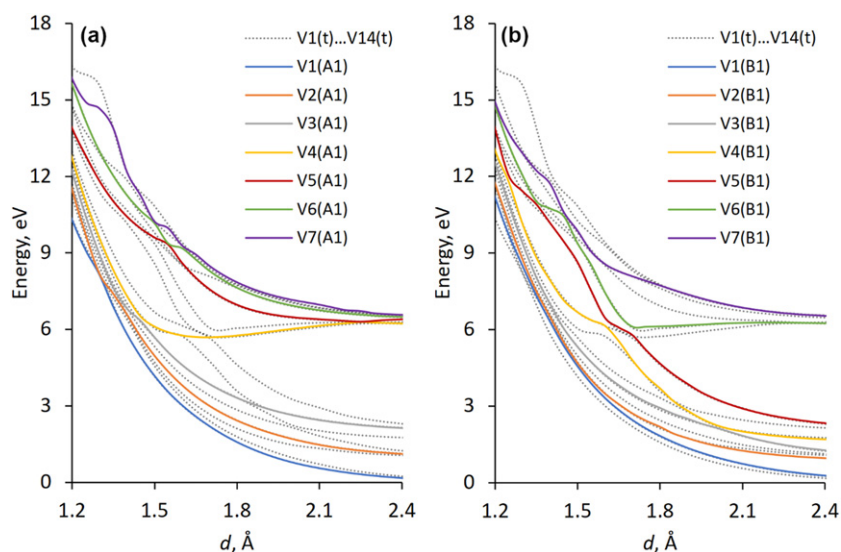
The initial diabatic state order can be assigned arbitrarily, but the ordering must be consistent over the entire geometric landscape. For example, if we assign a diabatic state ordering at geometry point P_1 , then follow a path to point P_2 such that the diabatic state ordering changes (as in the previous example), then continue along paths to point P_3 , P_4 , etc, along which paths the state ordering might or might not change, and eventually follow a path back to P_1 (closing a loop), we must get back to the original diabatic state order. Otherwise, a global surface fitting cannot be carried out. We handle this issue by carrying out the fitting in stages, and this section describes those stages.

First stage. First, we consider 1D paths. The locally avoided crossing of a pair of states along a 1D path can sometimes be recognized by visualization, and visualization was used to assign plausible diabatic state orderings as functions of the path coordinates. In principle, one could automate this by searching for local minima in the energy gaps between adiabatic curves, but this approach might require a quite dense data set along the path, and it is not guaranteed that all diabatic crossings are manifest as local minima in adiabatic gaps or that all minima in adiabatic gaps correspond to diabatic crossings. Properties like dipole moments, transition dipole moments, partial charges, or NACs can potentially also be used to try to identify the diabatic crossings, but for the present work, we mainly used visualization and the manual search for local minima in the adiabatic gaps.

We used 22 1D paths; the geometries of these paths are in table 4 (also see scheme 2). For 18 of the 22 1D paths, the geometries are described by Jacobi coordinates, where d is the distance between an atom and the center of mass of the remaining diatom, R is the diatomic distance, and γ is the angle between the diatomic axis and the vector from the atom to the center of mass on the diatom. For the remaining four 1D paths, two bond lengths (r_1 and r_2) and the bond angle (θ_3) of these two bonds describe the geometries. The fourteen adiabatic $^3A'$ potential energy curves along these 22 1D paths were plotted. As mentioned above, for the perpendicular-bisector and collinear paths, calculations with C_{2v} symmetry were also carried out, and we also plotted the potential energy curves of the 3A_1 and 3B_1 states of the C_{2v} symmetry calculations. These 1D plots were used

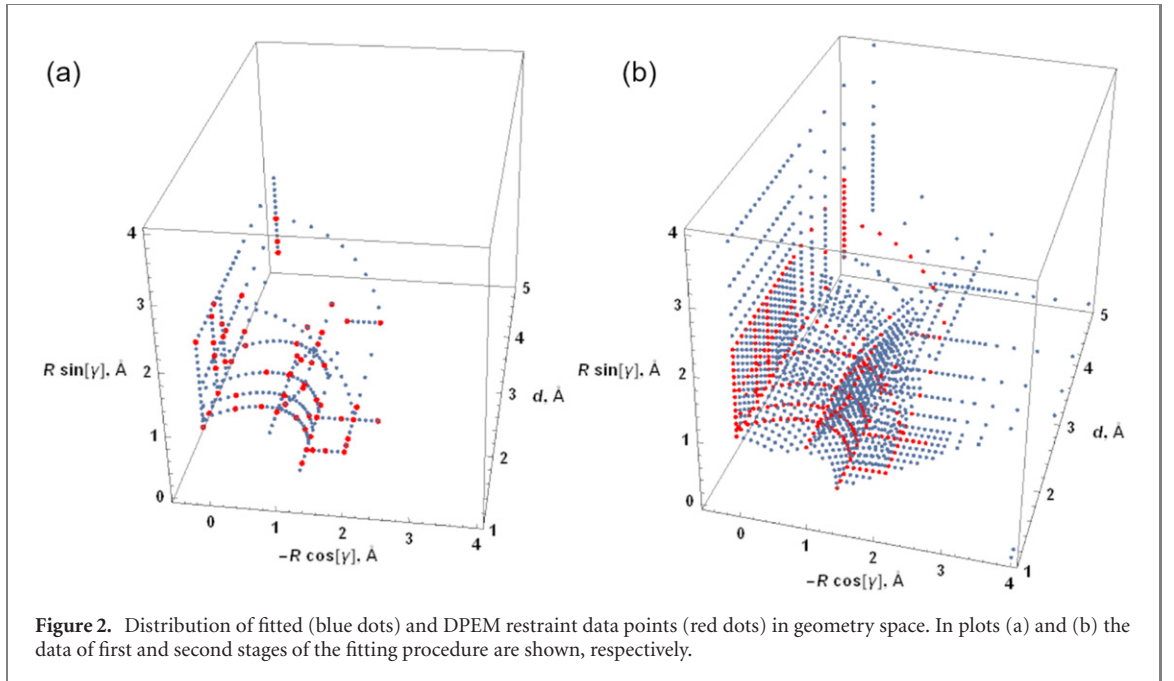
Table 4. Starting and ending geometries of the 22 1D paths.

#	Start { R (Å), d (Å), γ (deg)}	End { R (Å), d (Å), γ (deg)}	#	Start { R (Å), d (Å), γ (deg)}	End { R (Å), d (Å), γ (deg)}
1	{1.2, 1.0, 90}	{1.2, 4.0, 90}	17	{1.2, 1.3, 135}	{1.2, 3.0, 135}
2	{1.2, 1.5, 90}	{2.5, 1.5, 90}	18	{1.2, 1.6, 135}	{1.8, 1.6, 135}
3	{1.2, 1.8, 90}	{2.5, 1.8, 90}	19	{1.2, 2.3, 135}	{1.8, 2.3, 135}
4	{1.2, 1.0, 90}	{2.5, 1.0, 90}	20	{1.8, 1.6, 135}	{1.8, 3.0, 135}
5	{1.2, 4.0, 90}	{2.5, 4.0, 90}	21	{1.8, 2.3, 90}	{1.8, 2.3, 179}
6	{1.8, 1.0, 90}	{1.8, 4.0, 90}	22	{1.8, 4.0, 90}	{1.8, 4.0, 179}
7	{2.5, 1.0, 90}	{2.5, 4.0, 90}	#	Start	End
8	{1.2, 1.5, 179}	{1.2, 4.0, 179}		{ r_1 (Å), r_2 (Å), θ_3 (deg)}	
9	{1.2, 1.8, 179}	{1.8, 1.8, 179}	13	{1.2, 1.3, 60}	{1.2, 1.3, 180}
10	{1.2, 2.3, 179}	{2.2, 2.3, 179}	14	{1.2, 1.5, 60}	{1.2, 1.5, 180}
11	{1.8, 1.8, 179}	{1.8, 4.0, 179}	15	{1.2, 1.8, 60}	{1.2, 1.8, 180}
12	{1.2, 4.0, 179}	{1.8, 4.0, 179}	16	{1.2, 2.3, 60}	{1.2, 2.3, 180}

**Scheme 2.** Internal coordinates used in table 4.**Figure 1.** Calculated adiabatic energies along a path with $R = 1.2$ Å and $\gamma = 90$ deg. In panels (a) and (b) the 3A_1 and 3B_1 states are plotted, respectively, as solid curves; and in both panels all 14 ${}^3A'$ target potential energy curves, $V_1(t), \dots, V_{14}(t)$, are shown as dotted curves.

to figure out reasonable diabatic state orderings as functions of geometry. An example is shown in figure 1, where—for a perpendicular-bisector path—panels (a) and (b) show respectively the 3A_1 and 3B_1 calculations compared to the ${}^3A'$ potential energy curves. With plots like this, we used the GNU Image Manipulator Program (GIMP) [50], to assign a reasonable diabatic state order for all 22 1D paths.

Based on the diabatic state assignments of these 22 1D paths we selected 60 reference geometries as diabatic restraints (the second term on the right-hand side of equation (10)). For 58 of the 60 geometries, these diabatic potentials were equated to the adiabatic potentials (only the order of the adiabatic states is changed), and accordingly the diabatic coupling terms of these restraint geometries were set to zero. The remaining two geometries are at places where some states are strongly coupled. Because these strongly coupled state pairs are very close to their state crossings at the selected geometries, we made the energies of these coupled diabatic states equal to each other:



$$\mathbf{U}_{\kappa\kappa} = \mathbf{U}_{\lambda\lambda} = \frac{1}{2}(\mathbf{V}_{\kappa} + \mathbf{V}_{\lambda}) \quad (15)$$

$$\mathbf{U}_{\kappa\lambda} = \mathbf{U}_{\lambda\kappa} = \frac{1}{2}(\mathbf{V}_{\kappa} - \mathbf{V}_{\lambda}) \quad (16)$$

where κ and λ are indices of states. To keep the diabatic restraints simple, we assume that these coupled diabatic states are not coupled to other states. Therefore, the couplings in equations (15) and (16) do not affect the rest of the DPEM, where the diabatic energies are the (reordered) adiabatic energies with no coupling.

These 60 DPEM restraints are used in the fitting of adiabatic potentials along the of 22 1D paths, which contain 307 points (i.e., $J = 307$ in the first and fourth terms on the right-hand side of equation (10)). The geometry distribution of both the adiabatic fitting points and the DPEM restraint points are shown in figure 2(a). For these fits, the initial weights and biases were randomly generated, and for each network size, 50–200 runs were carried out. The best performing network had a (3,405,305,205,105) layer structure (in the notation defined after equation (14)). In this fit, the energies were not separated into two- and many-body terms and SPF input coordinates were used. The mean unsigned error (MUE) of the adiabatic energies is 86 meV in this fit. Although this fit could in principle predict the energies at any geometry, we are only interested in the diabatic energies of the 307 geometry points that are included in the fit. These diabatic energies will be used in stage 2.

Second stage. In stage 2, six 2D slices through the multidimensional space were fitted. These slices involve 1514 geometries and their adiabatic energies. The DPEM restraints in these fits are 303 diabatic energies and couplings from stage 1 (the other four points were left out because they did not produce good fits). The geometry distribution of both the adiabatic fitting points and the DPEM restraint points are shown in figure 2(b). The best performing fit for the 2D slices was obtained with the upgraded version of the PR-DDNN code. In this fit, the energies were not separated into two- and many-body terms and SPF input coordinates were used. The size of the network was kept at (3,405,305,205,105), and the weights and biases were randomly generated. The MUE of the adiabatic energies for this best fit is 22 meV.

Third stage. In stage 3, a preliminary global fit was carried out including 6340 data points. The DPEM restraints of this fit are the DPEMs of the 1514 geometries fitted in stage 2. In these fits, the energies were not separated into two-body and many-body terms, and SPF input coordinates were used. The network size remains at (3,405,305,205,105). The initial weights and biases were taken from best 2D fit, resulting in an MUE of 36 meV for the adiabatic energies. Many runs with randomly generated initial weights and biases were also considered, but they did not improve the fit. The (3,405,305,205,105) network consists of 208 790 weights and 1020 biases (see equations (12) and (13)).

Fourth stage. The objective of the fourth stage is to obtain a fit almost as good as the stage-3 fit, but with less neurons. In recent years, the reduction of the sizes of neural networks has received considerable attention, especially in commercial applications; see for example reference [51], where different techniques for reducing network size are collected. To reduce the size of stage-3 fit, all 6340 adiabatic data points were included, and all the 6340 fitted diabatic energies and couplings of the stage-3 fit were used as diabatic restraints. We then

Table 5. Mean unsigned errors (MUEs in meV) of the adiabatic energies and number of points (N) in different energy ranges (V in eV) of the final fit for fourteen ${}^3A'$ O_3 system.

	<5		5–10		10–20		20–40		>40		All
	N	MUE	N	MUE	N	MUE	N	MUE	N	MUE	MUE
V_1	6312	44	949	76	238	124	74	173	4	110	52
V_2	6087	40	1085	67	313	131	85	180	7	247	49
V_3	5831	39	1260	63	348	156	125	145	13	152	51
V_4	5582	33	1421	56	420	181	129	144	25	107	47
V_5	5230	32	1703	63	464	203	155	154	25	90	52
V_6	4931	29	1950	54	505	201	166	162	25	68	50
V_7	4615	32	2166	65	582	181	187	178	27	81	57
V_8	4195	29	2503	69	649	167	203	189	27	96	59
V_9	2102	55	4415	75	820	193	212	253	28	71	87
V_{10}	1815	30	4633	63	866	213	235	242	28	106	78
V_{11}	1435	32	4939	63	924	213	250	265	29	122	82
V_{12}	1197	28	4691	55	1200	191	460	201	29	250	82
V_{13}	713	29	5117	61	1189	217	529	216	29	277	94
V_{14}	621	42	5139	65	1216	200	571	266	30	180	101

systematically reduced the number of neurons in the network and checked the resulting MUEs for the adiabats with the goal of keeping the MUE of the new fit below 70 meV. For each tested network, usually two or three fits were made. In these test fits, the energies were not separated into two- and many-body terms and SPF input coordinates were used. The initial weights and biases were randomly generated. (The weights and biases of previous fits can only be used if the network size is not changed or is larger than that of the previous fit.) With this approach the size of the network was reduced to (3,15,35,55,105). In this smaller network, there are 8270 weights and 210 biases. Attempts to use even smaller networks resulted in significantly higher MUEs. We ran 25 fits with this-size network, and the three best MUEs of the adiabatic energies were 65, 66, and 69 meV.

We tested the computer time savings of using the (3,15,35,55,105) network instead of the (3,405,305,205,105) network by calculating energies and gradients at 10 000 geometries. For each network, this was repeated five times and the best time was picked to remove any delays caused by system loading. We found that the smaller network is about 6.5 times faster than the stage-3 network.

Fifth stage. Stage 5 led to the final fit. At this stage of the fitting, several changes were introduced. The two-body and many-body terms were separated so that the PR-DDNN method minimization is changed from equation (10) and (11). Since the SPF coordinates (equation (9a)) do not guarantee that the many-body term vanishes if the system is separated to an atom-diatom or atoms, we changed the input coordinates to exponentials (equation (9b)), and for similar reasons, we set all biases to zero and did not optimize them. To monitor the performances of these changes, new points were added to the data set for the $O_2 + O$ region. The target adiabatic data set was also extended with additional geometries to better describe geometries at the distances between the three oxygen atoms are very short; this was necessary because in test fits, this region the surfaces became unphysical. With these new points, the final fitting data set contains 7577 points. To obtain the final fit, the (3,15,35,55,105) network was used and the DPEM restraints are the same as in stage 4. The initial weights were randomly generated. With these settings, 50 fits were run, and the final fit was selected based on having both a good overall MUE (67 meV) and an especially good MUE for the lower-energy points. Table 5 shows the MUEs of the final fit for each state in five energy ranges.

Although one must be cautious about applying lessons learned in conventional regression to strategies when employing neural networks [52], and although the risk of over-fitting in deep neural networks is not simply measured by the number of weights and biases, we take this opportunity to compare the amount of data fit and the number of fitting parameters, since this still commands some attention in designing neural network strategies. The data for our final fit consists of 7577 sets of 14 adiabatic energies, which totals 106 078 data, and 6340 DPEM elements, which (since the DPEM is symmetric with 105 unique elements per geometry) totals 665 700 data. Adding these gives 771 778 data. The final fit has 8270 parameters (they are all weights since the 210 biases are not used in the final fit). Thus, the number of parameters is only 7.8% of the number of adiabatic energies and only 1.1% of the total amount of data.

In figure 3, the adiabatic and diabatic energies are shown for a selected perpendicular-bisector path ($R = 1.2 \text{ \AA}$, $\gamma = 90 \text{ deg}$). Panel (a) contains the target adiabatic energies of the fourteen ${}^3A'$ states; panel (b) contains the adiabatic energies of the final fit; and panel (c) contains the diabatic energies of the final fit. Panel (a) shows

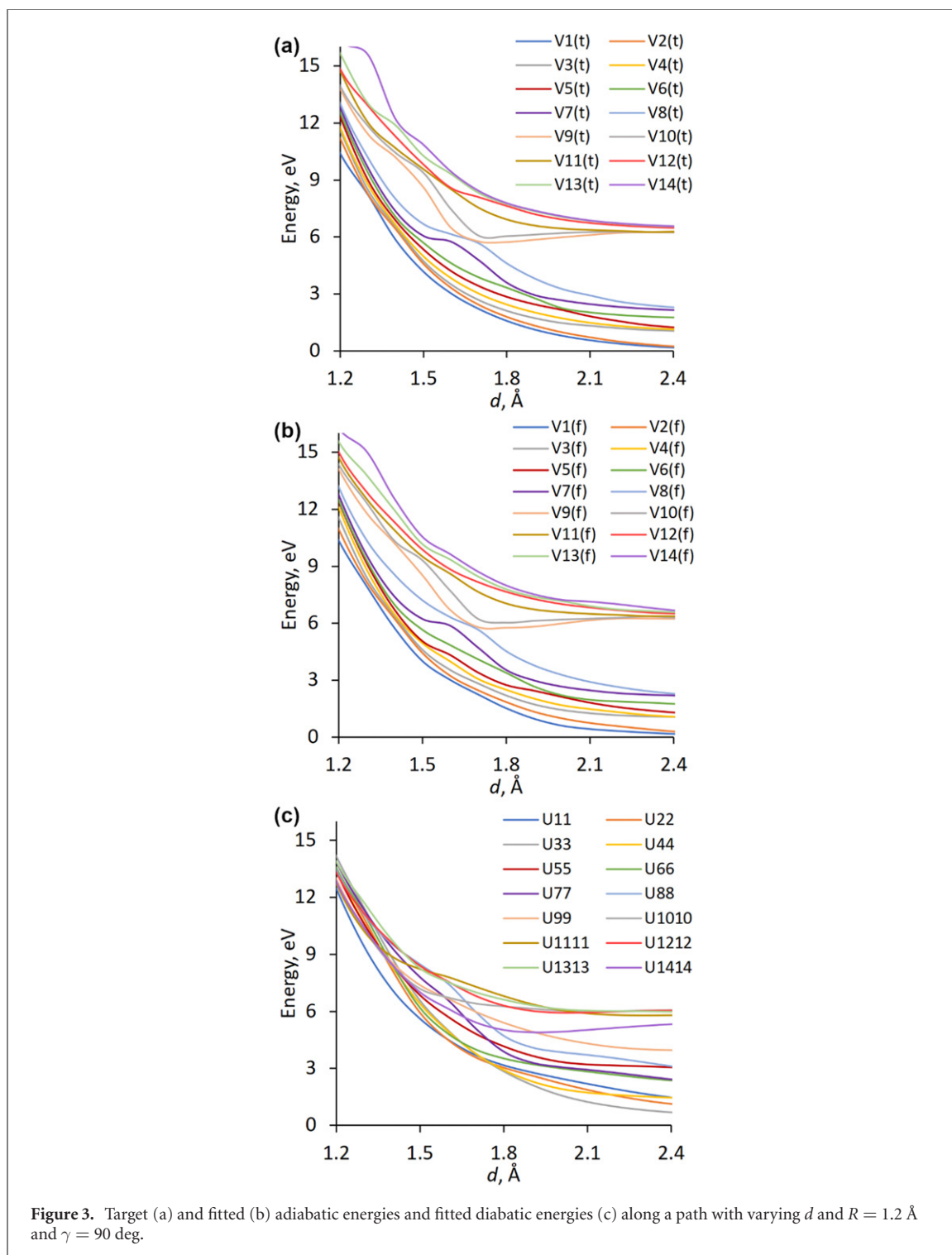


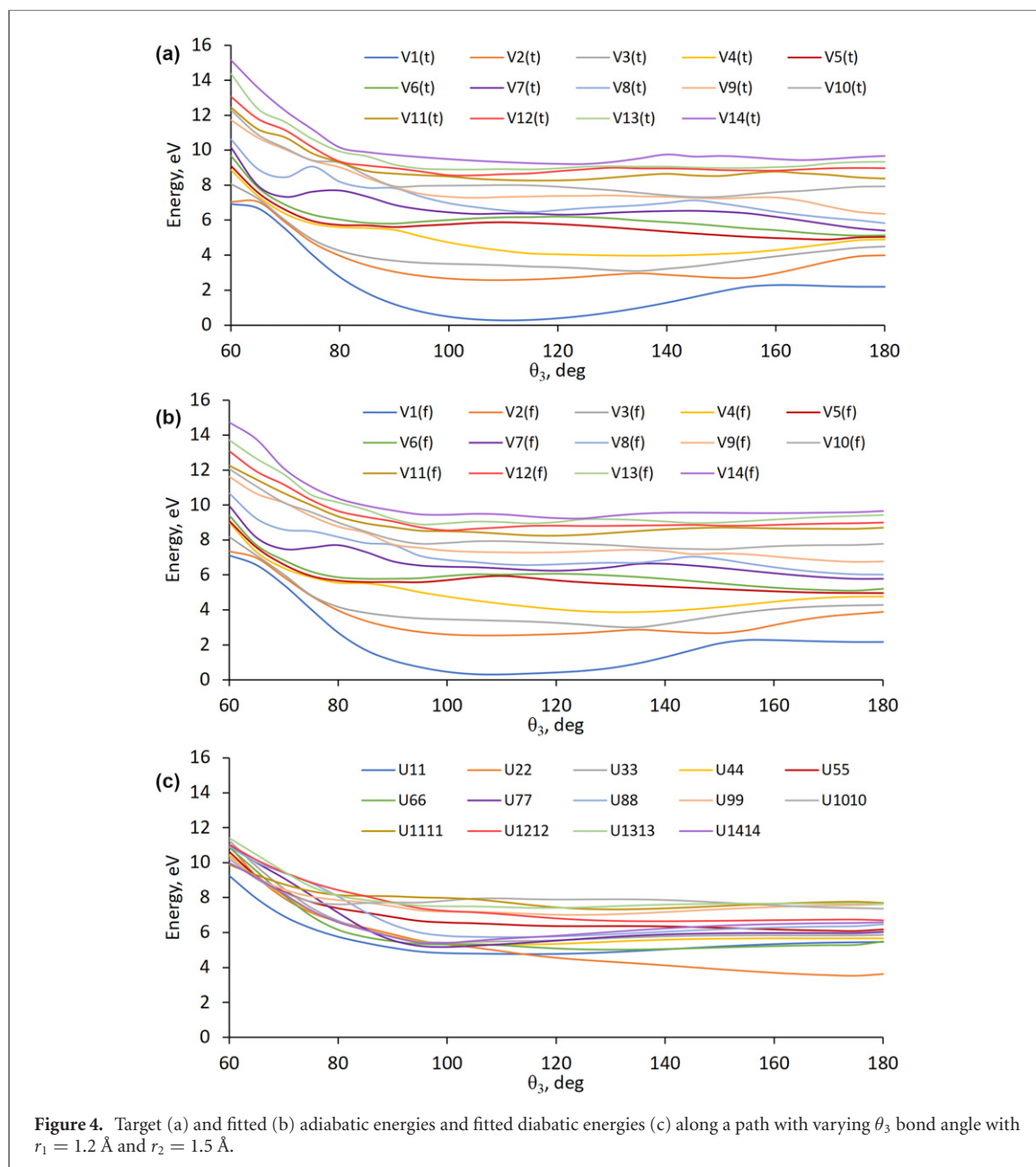
Figure 3. Target (a) and fitted (b) adiabatic energies and fitted diabatic energies (c) along a path with varying d and $R = 1.2$ Å and $\gamma = 90$ deg.

that the fourteen $^3A'$ adiabatic states have many locally avoided crossings. (The pattern is somewhat simplified if the A' states are distinguished as A_1 and B_1 states as was done in figure 1). The fitted adiabatic energies in panel (b) show good agreement with the target adiabatic energies in panel (a).

Figure 4 shows the adiabatic and diabatic energies along another path. In this case, the r_1 and r_2 bond lengths are fixed at 1.2 and 1.5 Å, respectively, and the θ_3 bond angle varies from 60 to 180 degrees. We see that the 14 fitted adiabatic energies show good agreement with the target adiabatic energies. The energy differences of the fitted and target adiabatic energies of each state for the paths shown in figures 3 and 4 can be seen in figures S1 and S2, respectively, in the supplementary material.

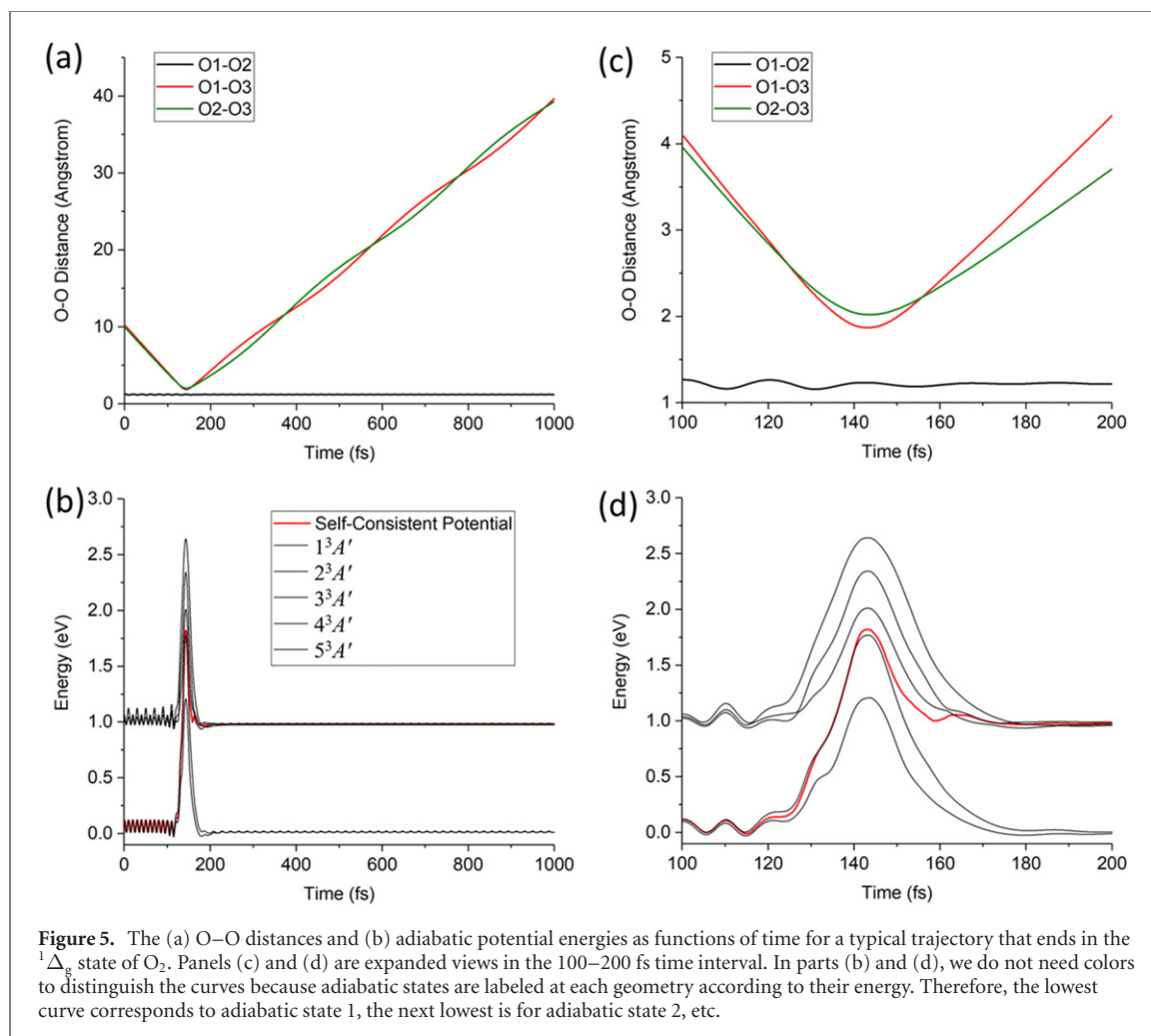
1.10. Electronically nonadiabatic collision dynamics

Having obtained a global DPDM, we next calculated nonadiabatic collision dynamics with the curvature-driven coherent switching with decay of mixing (κ CSDM) [53–55] semiclassical dynamics method, which involves



dynamics in the adiabatic representation. The κ CSDM method [54] is a version of the coherent switching with decay-of-mixing (CSDM) method [52] that requires as input only adiabatic potential energy surfaces and their gradients. In particular, it does not require either diabatic input or electronic calculations of NAC vectors or electronic wave function overlaps; instead, it obtains the effective NAC from the curvatures of the adiabatic potential energies along trajectory paths. This makes κ CSDM more efficient and more convenient than CSDM, and κ CSDM does not depend on the quality of the diabaticization in the PR-DDNN method. (This is an advantage because we believe that the fits to the adiabatic potential energy surfaces provided by PR-DDNN are more definitive than the diabatic potential energy matrices provided by PR-DDNN.) The CSDM algorithm is a semiclassical multi-state dynamics method that adds non-Markovian decoherence [56] to the semiclassical Ehrenfest [57, 58] method. CSDM has been validated in previous work [59, 60] against accurate quantum mechanical scattering calculations (we especially note that CSDM is more accurate than the widely used trajectory surface hopping [61] method), and κ CSDM retains the accuracy of the original more-demanding CSDM algorithm in tests carried out so far.

Two sets of initial conditions were considered, both involving the ground electronic states of O and O₂ and the initial rotational and vibrational quantum numbers of diatomic O₂ equal to 0, i.e., the ground state with zero-point vibrational energy. The two sets of initial conditions differ in the initial relative translational

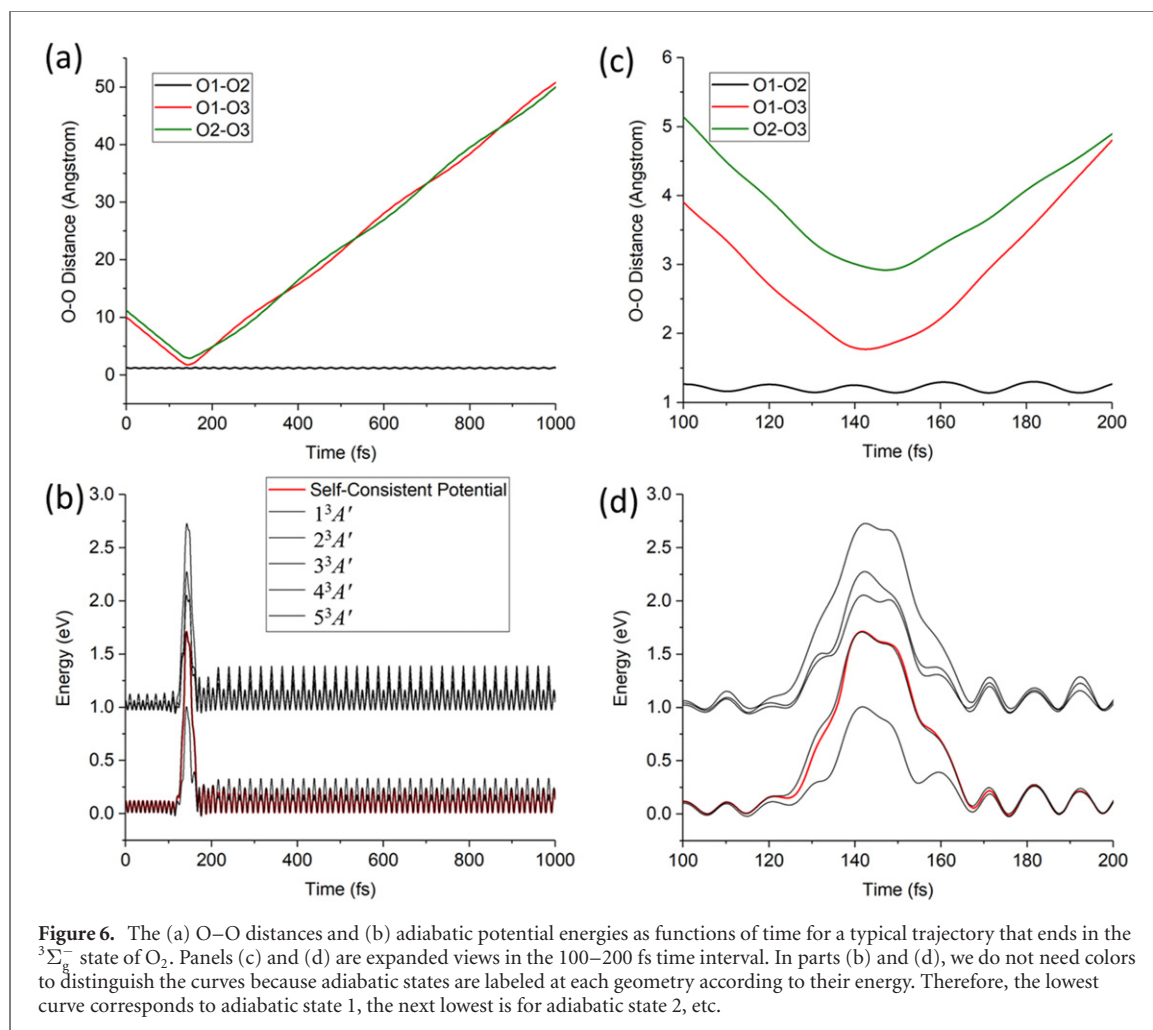


energy, which is equal to either 1.8 or 2.1 eV. Fourteen electronic states are coupled in the dynamics. Since the two lowest $^3A'$ states of O_3 both dissociate to ground-state $O + O_2$ (see table 1), half the trajectories were initiated on the $1^3A'$ surface and half on the $2^3A'$ surface.

The initial atom-diatom separation is set to 10 Å, and the impact parameter b is selected with stratified sampling from a $b db$ distribution. For each of the collision energies, we consider three ranges of impact parameter: 0–1 Å ($L = 1$), 1–2 Å ($L = 2$), and 2–3 Å ($L = 3$), where L denotes a range of impact parameters. An additional range of impact parameters, 3–4 Å ($L = 4$), is considered for initial relative translational energy equal to 2.1 eV. We ran 2000 trajectories for each range of impact parameters, with 1000 initialized on the $1^3A'$ surface, and another 1000 initialized on the $2^3A'$ surface. The initial nuclear coordinates and momenta were initialized by the initial condition sampling described elsewhere [62], as implemented in the ANT software [63]. These initial conditions were transformed into a format that is suitable for the SHARC-MN software [64], which was used for the dynamics. The curvature-driven effective NAC vector was projected to conserve the angular momentum of the system during the nonadiabatic collision process [65, 66]. The adaptive velocity-Verlet integrator was employed, with an initial nuclear time step of 0.1 fs, and 250 electronic substeps per nuclear step. To remove the small spurious asymptotic coupling that arises from using the Born–Oppenheimer states [67], we set the effective NAC and the corresponding time derivative coupling to exactly zero if any of the O–O distances is the greater than or equal to 4 Å. Total simulation time for each trajectory was 1 ps, by which time all collisions are completed, and the products are separating.

Figure 5 shows a typical trajectory for which the population ends in the $^1\Delta_g$ state of O_2 . Panels (a) and (c) of figure 5 show the three O–O distances as a function of time; panel (c) zooms in on the critical 100–200 fs time interval. Panels (b) and (d) of figure 5 show the energy of the self-consistent potential of κ CSDM and the energies of the first five electronic states.

Figure 6 is the same as figure 5 except for a typical trajectory that ends in the $^3\Sigma_g^-$ state of O_2 . Figure 5 shows less vibrational energy in the final O_2 molecule than is seen in figure 6, which is reasonable because a large fraction of the energy is tied up in electronic excitation energy in figure 5.



The fractional population on surface I is given by the diagonal element $\rho_{II}(t)$ of the electronic density matrix. After the collisions, we found very little population on surfaces 6–14; therefore, we concentrate the analysis on surfaces 1–5. The ensemble-averaged population of state I is computed by

$$\langle \rho_{II}^{(J)}(t) \rangle_L = \frac{1}{N_{\text{traj}}^{(J,L)}} \sum_{\xi=1}^{N_{\text{traj}}^{(J,L)}} \rho_{II}^{(J,L,\xi)}(t) \quad (17)$$

where $N_{\text{traj}}^{(J,L)}$ is the number of trajectories (1000 in the simulations reported here) beginning in state J in impact parameter range L , ξ is the index of a trajectory, and $\rho_{II}^{(J,L,\xi)}(t)$ is the population of electronic state I at time t for trajectory ξ of the batch starting in state J in b range L . Table 1 shows that the first two surfaces connect to the $^3\Sigma_g^-$ of O_2 , and the next three surfaces connect to the $^1\Delta_g$ state of O_2 ; therefore we calculated the ensemble-averaged population transfer $P(t)$ from $^3\Sigma_g^-$ to $^1\Delta_g$ as

$$\langle P(t) \rangle_L = \sum_{I=3}^5 \frac{\langle \rho_{II}^{(1)}(t) \rangle_L + \langle \rho_{II}^{(2)}(t) \rangle_L}{2} \quad (18)$$

In analyzing the trajectories, we distinguish nonreactive collisions in which the same two O atoms are bound after the collision as before from reactive collisions in which an exchange occurred. Experimentally distinguishing these types of collisions would require the use of isotopes, but theoretically it can be done to better understand the nature of the collisions (figure 7).

Table 6 presents—for the 1000 trajectories for each initial condition—the numbers of reactive trajectories, electronically inelastic collisions, and reactive electronically inelastic collisions and the averaged final rotational

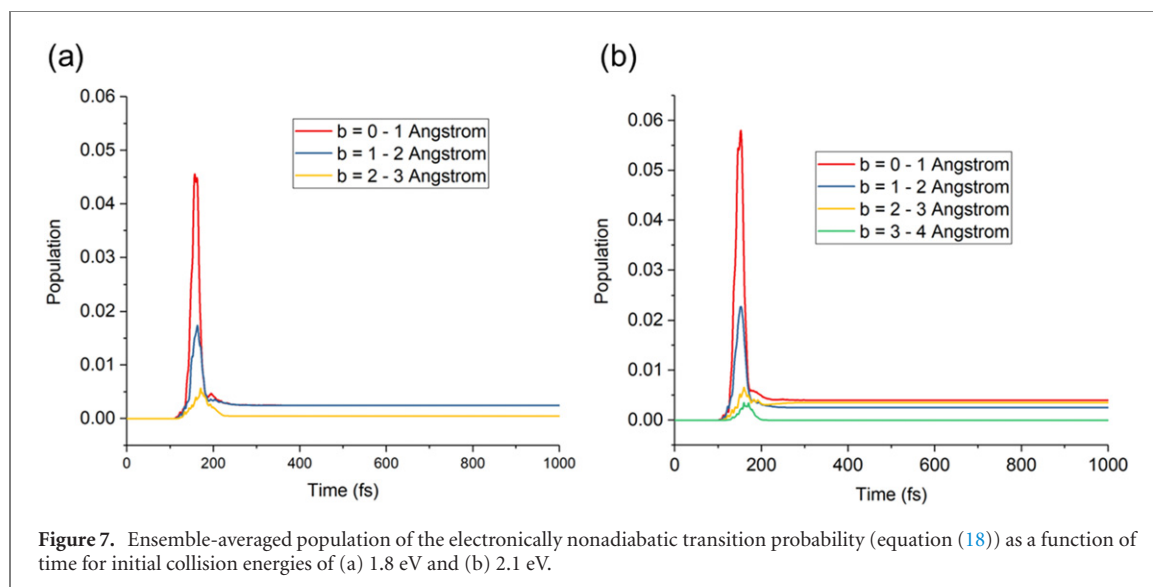


Figure 7. Ensemble-averaged population of the electronically nonadiabatic transition probability (equation (18)) as a function of time for initial collision energies of (a) 1.8 eV and (b) 2.1 eV.

Table 6. Number of reactive trajectories, number of trajectories that finish in $^1\Delta_g$ states, and number of reactive trajectories finish in $^1\Delta_g$ states for various initial conditions.

E_{rel} (eV)	Initial State	Impact parameter range L	Number of reactive trajectories	Trajectories that finish in $^1\Delta_g$	Reactive trajectories that finish in $^1\Delta_g$
1.8	$1^3A'$	1	458	2	1
	$2^3A'$	1	78	3	0
	$1^3A'$	2	176	3	0
	$2^3A'$	2	47	2	0
	$1^3A'$	3	0	0	0
	$2^3A'$	3	0	1	0
2.1	$1^3A'$	1	566	4	1
	$2^3A'$	1	77	4	0
	$1^3A'$	2	197	1	0
	$2^3A'$	2	50	4	0
	$1^3A'$	3	0	4	0
	$2^3A'$	3	0	3	0
	$1^3A'$	4	0	0	0
	$2^3A'$	4	0	0	0

Table 7. Probabilities, cross sections, and rate constants for electronically inelastic collisions in the $^3A'$ manifold.

E_{rel} (eV)	$\langle P(t) \rangle_1$	$\langle P(t) \rangle_2$	$\langle P(t) \rangle_3$	$\langle P(t) \rangle_4$	$\sigma(^1\Sigma_g^+ \rightarrow ^1\Delta_g)$ (\AA^2)	$k(^1\Sigma_g^+ \rightarrow ^1\Delta_g)$ ($\text{cm}^3 \text{mol}^{-1} \text{s}^{-1}$)
1.8	0.0025	0.0025	0.0005		0.039	2.2×10^{-12}
2.1	0.0040	0.0025	0.0035	0.000	0.091	5.5×10^{-12}

and vibrational energies. We compute the electronically inelastic cross section σ and rate constant k from the final ensemble average averages by stratified sampling:

$$\sigma(^3\Sigma_g^- \rightarrow ^1\Delta_g) = \pi \sum_{L=1}^3 (b_L^2 - b_{L-1}^2) \langle P(1 \text{ ps}) \rangle_L \quad (19)$$

$$k(^3\Sigma_g^- \rightarrow ^1\Delta_g) = v_{\text{rel}} \sigma(^3\Sigma_g^- \rightarrow ^1\Delta_g) \quad (20)$$

where $b_0 = 0$, $b_L = L \text{ \AA}$, and v_{rel} is the initial relative speed of collision. Table 7 gives the results. Similarly, the final ensemble averaged reactive cross section and rate constant is summarized in table 8.

2. Availability of surfaces and couplings

The Fortran subroutine of the fit of the 14 $^3A'$ states of O_3 is in the electronic supplementary information, and all the surfaces and couplings have also been added to the online POTLIB library [68, 69].

Table 8. Probabilities, cross sections, and rate constants for reactive collisions in the $^3A'$ manifold.^a

E_{rel} (eV)	$\langle P(\mathbf{t}) \rangle_1$	$\langle P(\mathbf{t}) \rangle_2$	$\langle P(\mathbf{t}) \rangle_3$	$\langle P(\mathbf{t}) \rangle_4$	$\sigma(\text{reactive})$ (\AA^2)	$k(\text{reactive})$ ($\text{cm}^3 \text{mol}^{-1} \text{s}^{-1}$)
1.8	0.27	0.11	0.00		1.9	1.1×10^{-10}
2.1	0.32	0.12	0.00	0.00	2.2	1.3×10^{-10}

^aNote that the tabulated cross sections and rate constants are calculated as if all collisions occur in the $^3A'$ manifold. As explained in the introduction, though, only 2/9 of the collisions occur in this manifold. Therefore, these contributions must be multiplied by 2/9 in computing their contribution to the physical cross sections and rate constants. The dynamical results presented here are just examples showing the usage of the coupled potential energy surfaces. A full study of the electronically inelastic cross sections and rate constants as functions of initial state, relative translational energy, or temperature is beyond the present scope.

3. Conclusions

In this work, we fitted the potential energy surfaces of the first 14 $^3A'$ states of O_3 system. To do that, we used the recently developed PR-DDNN method with a multi-stage approach. In these stages, larger and larger portions (selected 1D cuts, selected 2D cuts, ...) of the global O_3 surfaces are fitted, where the diabatic restraints for a given stage are based on the fits of a previous stage and at the first stage the diabatic restraints are obtained manually. The fitted DPEMs of 14 $^3A'$ states of O_3 system can be used directly or with straightforward transformation to obtain adiabatic data for dynamics simulations. We carried out collision dynamics in the adiabatic representation with κCSDM to illustrate the usage of the surfaces. In these example dynamics, we calculated cross sections for excitation of ground-state O_2 in $^3A'$ collisions with ground-state O.

Acknowledgments

This work was supported in part by the Air Force Office of Scientific Research by Grant FA9550-19-1-0219.

Conflict of interest

There are no conflicts to declare.

Data availability statement

All data that support the findings of this study are included within the article (and any supplementary files).

Appendix A. Geometries where adiabatic energies were calculated

For most of the triatomic calculations with C_s symmetry, the Jacobi coordinates of an atom–diatom system were used. The bond length R of the diatom was set to a value in the range 0.9–2.5 \AA with a 0.1 \AA increment plus 2.7, 3.0, 3.4, and 4.0 \AA . For the distance d between the atom and the center of mass of the diatom, the values are set in the range 1.0–2.5 \AA with 0.1 \AA increment plus 2.7, 3.0, 3.4, 4.0, and 5.0 \AA . Each d value was combined with each R value at a given value of the angle γ between the diatomic axis and the vector from the atom to the center of mass on the diatom. For $d \leq 3.0$ \AA , the angle γ was set to 90–175 deg with a 5 deg increment plus 179 deg. For $d = 3.4$ and 4.0 \AA , γ was set to 90–170 deg with a 10 deg increment plus 179 deg. For $d = 5.0$ \AA , γ was set to 90, 120, 150, and 179 deg. This is called the multidimensional grid. If any of the three internuclear distances is less than 0.9 \AA , then that multidimensional grid point is skipped. We note that the potentials at large distances are entirely described by the pairwise potentials in the final fits.

We then added some geometries with at least one very short bond length. For this we set $\gamma = 90, 120, 150,$ and 179 deg, and for each γ , we considered two set of geometries: with $d = 0.8$ \AA , we set $R = 0.8, 1.0, 1.2, 1.4, 1.6, 1.8, 2.0, 2.2, 2.5,$ and 2.7 \AA ; and with $d = 0.7$ \AA , we set $R = 1.8, 2.0, 2.2, 2.5,$ and 2.7 \AA .

We also added some cuts where two internuclear distances (r_1 and r_2) and the bond angle (θ_3) between those two bonds were used to define the geometry. In these calculations, $r_1 = 1.2$ \AA , θ_3 is set to 60–180 deg with a 5 deg increment, and r_2 is set to 1.3, 1.5, 1.8 \AA , and 2.3 \AA .

Appendix B. Special procedures for potential curves leading to O(¹D)

The asymptotically degenerate $n = 7, 8$ potentials dissociate to the ground state of O₂ combined with the excited ¹D state of the atom (see table 1). This requires a special procedure to fit the associated O₂ potential because the O(³P) + O(³P) + O(¹D) energy level is not among the calculated fourteen lowest-energy states because all fourteen ³A' states of the O₃ system dissociate to the ground energy level of three O(³P) atoms. This appendix describes a three-segment procedure that we used to handle the diatomic curve used for $n = 7$ and 8.

For the first segment, the energy of the O₂(³Σ_g⁻) potential energy curve is shifted by the energy difference of the ¹D and ³P states of O atom. This was accomplished as follows. Using the potential energy curve of O₂(³Σ_g⁻) from our previous work (mentioned above), we calculated the V^{SR} energy of the curve between 0.6 and 1.55 Å with a 0.05 Å increment and between 1.20 and 1.22 Å with a 0.001 Å increment; and the energy shift of the ¹D and ³P states of O atom (1.97 eV) were added to these energies.

But the potential curve shifted by the energy difference of the ¹D and ³P states of O atom would dissociate to an asymptote not included in the first fourteen states. By definition, the MB term must vanish where less than three atoms are interacting in the O₃ system; therefore, a mixed potential energy curve is constructed for $n = 7, 8$. In this mixed potential energy curve, the short-distance part (<1.6 Å) is the first segment described in the previous paragraph. Then, for the middle distances (1.6–2.1 Å), where the dissociation curve of O₂ for state ³Σ_g⁻ energetically shifted up by excitation energy of O(¹D) crosses with the potential energy curves that lead to three O(³P) atoms, the energies of this mixed potential were taken from the fourteen-state calculations of O₃, and in particular we used the energies of the 13th adiabatic state with the third atom is placed 9 Å apart from the diatom. The $V^{\text{D}^{3(\text{BJ})}}$ energies were subtracted from energies of the 13th state to get the V^{SR} contribution for the fit.

For longer distances (≥2.15 Å) of this potential energy curve, the V^{SR} part of the already fitted O₂(³Σ_g⁻) potential was used. The V^{SR} energies were calculated between 2.15 and 9 Å with 0.05 Å increment for this part of the curve.

These three segments (short-distance, middle-distance, and long-distance) were then fitted as a single curve. The crossing of the potential energy curve that dissociates to the O(³P) + O(³P) + O(¹D) energy level with the curve that dissociate to three O(³P) atoms occurs in the middle-distance segment around 1.7 Å. Since, only the lower-energy curve is considered at this crossing, the crossing leads to a sudden change of the first derivative of the curve that the even-tempered Gaussian expression cannot fit that; therefore, the functional form was extended with an additional Gaussian function centered at 1.7 Å as shown in equation (5) for $n = 7, 8$.

ORCID iDs

Zoltan Varga  <https://orcid.org/0000-0002-9324-798X>

Yinan Shu  <https://orcid.org/0000-0002-8371-0221>

Jiaxin Ning  <https://orcid.org/0000-0003-0305-607X>

Donald G Truhlar  <https://orcid.org/0000-0002-7742-7294>

References

- [1] Shu, Varga, Kanchanakungwankul, Truhlar and Truhlar 2022 *J. Phys. Chem. A* **126** 992
- [2] Grover, Schwartztruber and Schwartztruber 2019 *Phys. Fluids* **31** 076107
- [3] Kulkarni, Truhlar, Goverapet Srinivasan, van Duin, Schwartztruber and Schwartztruber 2013 *J. Phys. Chem. A* **117** 258
- [4] Candler 2019 *Annu. Rev. Fluid Mech.* **51** 379
- [5] Varga, Truhlar and Truhlar 2017 *J. Chem. Phys.* **147** 154312
- [6] Grover, Schwartztruber, Truhlar and Truhlar 2019 *J. Thermophys. Heat Transfer* **33** 797
- [7] Pan, Stephani and Stephani 2019 *J. Chem. Phys.* **150** 074305
- [8] Grover and Schwartztruber 2019 *AIP Conf. Proc.* **2132** 090005
- [9] Subramaniam and Stephani 2019 *AIP Conf. Proc.* **2132** 150004
- [10] Andrienko 2020 *J. Chem. Phys.* **152** 044305
- [11] Venturi, Panesi and Panesi 2020 *J. Phys. Chem. A* **124** 5129
- [12] Venturi, Sharma, Panesi and Panesi 2020 *J. Phys. Chem. A* **124** 8359
- [13] Subramaniam, Stephani and Stephani 2020 *Phys. Rev. Fluids* **5** 113402
- [14] Schwartztruber and Schwartztruber 2020 *J. Chem. Phys.* **153** 184302
- [15] Privat, Honvault and Honvault 2021 *J. Chem. Phys.* **154** 104303
- [16] Stephani and Stephani 2021 *J. Chem. Phys.* **154** 104306
- [17] Zhang, Cheng and Cheng 2022 *Russ. J. Phys. Chem.* **96** 876

- [18] Jasper, Kendrick, Truhlar and Truhlar 2004 *Non-Born–Oppenheimer Chemistry: Potential Surfaces, Couplings, and Dynamics in Modern Trends in Chemical Reaction Dynamics: Experiment and Theory (Part 1)* ed X Yang and K Liu (Singapore: World Scientific) pp 329–91
- [19] Huber and Herzberg 1979 *Molecular Spectra and Molecular Structure: IV. Constants of Diatomic Molecules* (New York: Van Nostrand Reinhold)
- [20] Kramida, Ralchenko and Reader (NIST ASD Team) 2020 *NIST Atomic Spectra Database (Ver. 5.8)* National Institute of Standards and Technology Gaithersburg, MD (<https://physics.nist.gov/asd> (accessed 26 August 2021))
- [21] Truhlar 1972 Multiple potential energy surfaces for reactions of species in degenerate electronic states *J. Chem. Phys.* **56** 3189
- [22] Truhlar 1974 *J. Chem. Phys.* **61** 440 (erratum)
- [23] Truhlar and Truhlar 2012 *J. Chem. Phys.* **137** 22A539
- [24] Ndengué, Quintas-Sánchez, Osborn and Osborn 2021 *J. Phys. Chem. A* **125** 5519
- [25] Truhlar and Truhlar 2020 *J. Chem. Theory Comput.* **16** 6456
- [26] Shu, Varga, Sampaio de Oliveira-Filho and Truhlar 2021 *J. Chem. Theory Comput.* **17** 1106
- [27] Granovsky 2011 *J. Chem. Phys.* **134** 214113
- [28] Shiozaki, Györfy, Celani and Werner 2011 *J. Chem. Phys.* **135** 081106
- [29] Ruedenberg, Elbert and Elbert 1979 *Int. J. Quantum Chem.* **16** 1069
- [30] Roos, Sigbahn and Siegbahn 1980 *Chem. Phys.* **48** 157
- [31] Roos, Zimmermann A and Keller H U 1987 *Adv. Chem. Phys.* **88** 399
- [32] Malmqvist and Malmqvist 1997 *Chem. Phys. Lett.* **274** 196
- [33] Ghigo, Roos and Malmqvist 2004 *Chem. Phys. Lett.* **396** 142
- [34] Dunning and Dunning Jr. 2002 *J. Chem. Phys.* **117** 10548
- [35] Papajak, Leverentz, Truhlar and Truhlar 2009 *J. Chem. Theory Comput.* **5** 1197
- [36] Galván I F et al 2019 *J. Chem. Theory Comput.* **15** 5925
- [37] Aquilante et al 2020 *J. Chem. Phys.* **152** 214117
- [38] Li, Varga, Truhlar and Guo 2020 *J. Chem. Theory Comput.* **16** 4822
- [39] Paukku, Yang, Varga, Song, Truhlar and Truhlar 2017 *J. Chem. Phys.* **147** 034301
- [40] Varga, Liu, Li, Paukku, Truhlar and Truhlar 2021 *J. Chem. Phys.* **154** 084304
- [41] Grimme, Antony, Krieg and Krieg 2010 *J. Chem. Phys.* **132** 154104
- [42] Grimme, Goerigk and Goerigk 2011 *J. Comput. Chem.* **32** 1456
- [43] Verma, Wang, Truhlar and Truhlar 2017 *J. Phys. Chem. A* **121** 2855
- [44] Bytautas, Ruedenberg and Ruedenberg 2010 *J. Chem. Phys.* **132** 074307
- [45] Truhlar and Truhlar 1985 *Chem. Phys. Lett.* **117** 307
- [46] Paszke et al 2019 PyTorch: an imperative style, high-performance deep learning library *Advances in Neural Information Processing Systems* vol 32 ed H Wallach, H Larochelle, A Beygelzimer, F d'Alché-Buc, E Fox and , R Garnett (Vancouver, BC: Curran Associates, Inc.) pp 8024–35
- [47] Nocedal and Nocedal 1989 *Math. Program.* **45** 503
- [48] Hendrycks and Gimpel 2016 Bridging nonlinearities and stochastic regularizers with Gaussian (arXiv:1606.08415)
- [49] Simons, Finlan and Finlan 1973 *J. Chem. Phys.* **59** 3229
- [50] Rumelhart, Williams and Williams 1986 *Nature* **323** 533
- [51] Kimball and Mattis (GIMP Development Team) 2021 GIMP, version 2.10.24 (<https://gimp.org>)
- [52] Cheng, Wang, Zhang and Zhang 2018 *IEEE Signal Process. Mag.* **35** 126
- [53] Belkin, Hsu, Ma and Mandal 2019 *Proc. Natl Acad. Sci. USA* **116** 15849
- [54] Zhu, Nangia, Truhlar and Truhlar 2004 *J. Chem. Phys.* **121** 7658
- [55] Shu, Zhang, Mai, Sun, Truhlar and Truhlar 2020 *J. Chem. Theory Comput.* **16** 3464
- [56] Shu, Zhang, Chen, Sun, Truhlar and Truhlar 2022 *J. Chem. Theory Comput.* **18** 1320
- [57] Zhu, Truhlar and Truhlar 2005 *J. Chem. Theory Comput.* **1** 527
- [58] Meyer and Miller 1979 *J. Chem. Phys.* **70** 3214
- [59] Topaler, Allison, Truhlar and Truhlar 1998 *J. Chem. Phys.* **109** 3321
- [60] Jasper, Nangia, Truhlar and Truhlar 2006 *Acc. Chem. Res.* **39** 101
- [61] Truhlar 2007 Decoherence in combined quantum mechanical and classical mechanical methods for dynamics as illustrated for non-Born–Oppenheimer trajectories *Quantum Dynamics of Complex Molecular Systems* ed D A Micha and I Burghardt (Berlin: Springer) pp 227–43
- [62] Tully J C 1990 *J. Chem. Phys.* **93** 1061
- [63] Muckerman and Muckerman 1979 Reactive scattering cross sections III: quasiclassical and semiclassical methods *Atom-Molecule Collision Theory: A Guide for the Experimentalist* ed R B Bernstein (New York: Plenum Press) pp 505–66
- [64] Zheng, Li, Jasper, Bonhommeau, Valero, Meana-Pañeda, Mielke, Zhang and Truhlar 2019 *ANT, Version 2019* (Minneapolis: University of Minnesota)
- [65] Shu, Zhang and Truhlar 2022 *SHARC-MN-v1.2* (Minneapolis: University of Minnesota)
- [66] Shu, Zhang, Truhlar and Truhlar 2020 *J. Chem. Theory Comput.* **16** 4098
- [67] Shu, Zhang, Varga, Parker, Kanchanakungwankul, Sun and Truhlar 2020 *J. Phys. Chem. Lett.* **11** 1140
- [68] Truhlar and Truhlar 1981 The coupling of electronically adiabatic states in atomic and molecular collisions *Theoretical Chemistry: Advances and Perspectives Theory of Scattering: Papers in Honor of Henry Eyring vol 6A* ed D Henderson (New York: Academic) pp 215–89
- [69] Duchovic, Volobuev, Lynch, Truhlar, Allison, Wagner, Corchado and Garrett 2002 *Comput. Phys. Commun.* **144** 169
- [70] Duchovic, Volobuev, Lynch, Truhlar, Allison, Wagner, Corchado and Garrett 2004 *Comput. Phys. Commun.* **156** 319 (erratum)
- [71] Duchovic et al 2022 POTLIB: an online library of potential energy surfaces (<https://comp.chem.umn.edu/potlib/> (accessed 1 August 2022))